ARTICLE

Hydrated Alkali-$B_{11}H_{14}$ Salts as Potential Solid-State Electrolytes†

Diego H. P. Souza,[a] Kasper T. Møller,[ab] Stephen A. Moggach,[c] Terry D. Humphries,[a] Anita M. D'Angelo,[d] Craig E. Buckley,[a] and Mark Paskevicius*[a]

Received 00th January 20xx,
Accepted 00th January 20xx

DOI: 10.1039/x0xx00000x

Metal boron-hydrogen compounds are considered as promising solid electrolyte candidates for the development of all-solid-state batteries (ASSB), owing to the high ionic conductivity exhibited by *closo*- and *nido*-boranes. In this study, an optimised low cost preparation method of $MB_{11}H_{14}\cdot(H_2O)_n$, ($M$ = Li and Na) and $KB_{11}H_{14}$ is proposed and analysed.The formation of the $B_{11}H_{14}^-$ salt is pH-dependent, and H_3O^+ competes with small ionic radii cations, such as Li^+ and Na^+, to produce a hydronium salt of $B_{11}H_{14}^-$, which forms $B_{11}H_{13}OH^-$ upon heating. The use of diethyl ether to extract $B_{11}H_{14}^-$ salt from the aqueous medium during synthesis is an important step to avoid hydrolysis of the compound upon drying. The proposed method of synthesis results in $LiB_{11}H_{14}$ and $NaB_{11}H_{14}$ coordinated with water, whereas $KB_{11}H_{14}$ is anhydrous. Hydrated $LiB_{11}H_{14}\cdot(H_2O)_n$ and $NaB_{11}H_{14}\cdot(H_2O)_n$ exhibit exceptional ionic conductivities at 25 °C, 1.8 x 10^{-4} S·cm^{-1} and 1.1 x 10^{-3} S·cm^{-1}, respectively, which represent some of the highest solid-state Li^+ and Na^+ conductivities at room temperature. The salts also exhibit oxidative stability of 2.1 V vs. Li^+/Li and 2.6 V vs. Na^+/Na, respectively. $KB_{11}H_{14}$ undergoes a reversible polymorphic structural transition to a metastable phase before decomposing. All synthesised *nido*-boranes decompose at temperatures greater than 200 °C.

INTRODUCTION

The use of natural resources, such as the sun, wind, or waves, is a clean and sustainable strategy to replace fossil fuels and to produce renewable energy. However, these sources of power are intermittent, which make them incapable of fulfilling the demands of base-load energy usage. One way to address this problem is to develop more efficient and low cost energy storage devices, such as batteries, to be coupled with renewable sources and allow continuous electricity supply.[1–3]

The drawbacks of state-of-the-art lithium-ion batteries, such as the use of toxic and flammable liquid organic electrolytes, along with the risks of leakage, freezing, and vaporization of the organic component, have led to extensive research on the development of all-solid-state-batteries (ASSBs), which are considered the next-generation electrochemical storage device.[4–7] Furthermore, the energy density of a battery cell can be increased with the use of solid electrolytes, as they are compatible with alternative electrode materials, e.g. lithium metal, which is considered the ultimate anode for ASSBs. Lithium has a low standard half-cell potential (–3.04 V vs. standard hydrogen electrode) and a high theoretical capacity (3860 mAh·g^{-1}), thus the energy density of the battery can be increased significantly.[8,9] Another advantage that ASSBs bring is that they are easier to miniaturize, as the electrolyte is no longer a liquid.[7]

The first challenge in building an ASSB is to develop a solid-state electrolyte with high ionic conductivity at room temperature (≥ 1 x 10^{-3} S·cm^{-1}). The electrolyte must be an electrical insulator, inert, be compatible with the anode and cathode materials, and possess a wide electrochemical stability window capable of covering the working potential of the cell.[7,10] Many different classes of materials have been studied, including, but not limited to, polymers,[11,12] metal oxides,[13,14] sulfides,[15–17] and metal boron-hydrogen compounds.[18–21] The latter have recently drawn attention from several research groups due to their ability to adopt a disordered crystallographic structure at elevated temperature that leads to superionic conductivity.[22] Additionally, complex metal hydrides are strong reducing agents and generally electrochemically stable against a metallic lithium or sodium anode. Sodium and potassium batteries are under strong consideration to replace lithium batteries due to the high abundance and lower cost of both metals.[23,24] To ensure a viable and affordable large-scale production of the battery, it is important to find an electrolyte with a low materials and synthesis cost.

Nido-boranes, boron-hydrogen anions with a nest like structure, can form impressive ionic conducting salts with Na^+ cations.[21,25] Pathways for producing the metal *nido*-boranes $MB_{11}H_{14}$, M = Li, Na, or K, free of ethereal solvent, have not been clearly elucidated. In previous research, $NaB_{11}H_{14}$ was commercially obtained,[21] and its ionic conductivity was considerably high at room temperature (~1 x 10^{-3} S·cm^{-1}).

[a] Department of Physics and Astronomy, Fuels and Energy Technology Institute, Curtin University, GPO Box U1987, Perth, WA 6845, Australia.
[b] Department of Biological and Chemical Engineering, Aarhus University, Aabogade 40, Aarhus, DK-8200, Denmark.
[c] School of Molecular Sciences, The University of Western Australia (M310), Crawley, WA 6009, Australia; Centre for Microscopy, Characterization and Analysis, The University of Western Australia, Perth, WA 6009, Australia.
[d] Australian Synchrotron (ANSTO), Clayton, VIC 3168, Australia

†Electronic Supplementary Information (ESI) available: Experimental details. XRPD, TDA-MS, TGA-DSC, LSV, TPPA data. Rietveld refinement, *In-situ* synchrotron PXRD plots and SC-XRD data. CSD 2090015 and CSD 2031335. Nyquist and ionic conductivity plots. Experimental and DFT calculated multinuclear NMR and FTIR spectroscopic data. DFT Calculated data for $B_{11}H_{14}^-$ and $B_{11}H_{13}OH^-$ including atomic coordinates, bond lengths and angles, and NPA analysis. See DOI: 10.1039/x0xx00000x

However, the $NaB_{11}H_{14}$ was drastically different in terms of its structure and properties when supplied from two different batches from the same company.[21] Another study on the synthesis of $NaB_{11}H_{14}$ lacks certain synthetic details on concentration of reactants and pH that are vital in preparing this material.[25] In addition, the ionic conductivity measurements for commercially supplied $NaB_{11}H_{14}$ and for $NaB_{11}H_{14}$ synthesised using decaborane are published, but not for the compound synthesised from diglyme, leading to concerns over its purity and yield.[25] This highlights how difficult it can be to achieve a reproducible and reliable synthesis of $MB_{11}H_{14}$ (*M* = Li, Na, K). In previous research, there is also no clear evidence of the analysed borane salt being solvated by, e.g. water.[21,25] Herein, the synthesis of $LiB_{11}H_{14}\cdot(H_2O)_n$, $NaB_{11}H_{14}\cdot(H_2O)_n$ and $KB_{11}H_{14}$, free of diglyme, through a facile, cheap, and safe synthetic route to be mass-produced is presented, alongside the electrochemical properties, the structural features, and the trends in thermal behaviour.

EXPERIMENTAL

Chemicals

Sodium borohydride ($NaBH_4$, anhydrous, 98%), diglyme ($C_6H_{14}O_3$, anhydrous, 99.5%), 1-bromopentane ($C_5H_{11}Br$, 98%), diethyl ether ($(C_2H_5)_2O$, anhydrous, 99.7%), trimethylamine hydrochloride ($(CH_3)_3N\cdot HCl$, 98%), potassium hydroxide (KOH, 90%), sulfuric acid (H_2SO_4, 95–98%), deuterated water (D_2O, 99.9 atom % D), deuterated dimethyl sulfoxide (DMSO-d_6, anhydrous, 99.9 atom % D), deuterated acetonitrile (CD_3CN, 99.8 atom % D), lithium (Li ribbon, thickness 0.38 mm, 99.9%), sodium (Na lump in kerosene, 99%), and graphite powder were all purchased from Sigma-Aldrich. Lithium hydroxide (LiOH, anhydrous, 98%) and gold foil (Au, 99.95%, thickness 0.1 mm) were obtained from Alfa Aesar, sodium hydroxide (NaOH, 98.9%) from VWR Chemicals, and hydrochloric acid (HCl, 37%) from Scharlau. In order to maintain an inert atmosphere, all chemicals and samples were manipulated in an argon filled glovebox (Mbraun, O_2 & H_2O < 1 ppm) or using Schlenk techniques.

Synthesis of trimethylammonium *nido*-tetradecahydroundecaborane, $(CH_3)_3NHB_{11}H_{14}$

$$11NaBH_{4(s)} + 10C_5H_{11}Br_{(l)} \xrightarrow{C_6H_{14}O_3,\ 110\ ^\circ C} NaB_{11}H_{14}\cdot(C_6H_{14}O_3)_{n(sol)} + 10NaBr_{(s)} + 10C_5H_{12(g)} + 10H_{2(g)} \quad (1)$$

$$NaB_{11}H_{14}\cdot(C_6H_{14}O_3)_{n(aq)} + (CH_3)_3N\cdot HCl_{(aq)} \xrightarrow{H_2O,\ 25\ ^\circ C} (CH_3)_3NHB_{11}H_{14(s)} + NaCl_{(aq)} + n(C_6H_{14}O_3)_{(aq)} \quad (2)$$

The syntheses of $NaB_{11}H_{14}\cdot(C_6H_{14}O_3)_n$ and $(CH_3)_3NHB_{11}H_{14}$ (eq. 1 and 2) were performed based on methods previously reported by Dunks *et al.*[26] and Muetterties *et al.*[24] with adaptations. $NaBH_4$ (50 g, 1.32 mol) was weighed into a three-neck round-bottom flask equipped with a thermometer, a mechanical stirrer, and a pressure-equalizing dropping funnel. Under stirring, and a constant stream of argon, the powder was suspended in diglyme (400 mL) and heated to 105 °C. 1-bromopentane (150 mL, 1.20 mol) was added drop-wise to ensure that the temperature was kept between 105 and 120 °C (exothermic reaction). After complete addition, the reaction mixture was stirred for six additional hours at 110 °C. The resulting suspension of yellow liquid and white powder (undissolved NaBr) was cooled to room temperature, filtered, and washed with about 50 mL of diethyl ether. The filtrate was dried *in vacuo* at 110 °C until a gelatinous yellow substance (40.5 g) was obtained. This yellow substance was then completely dissolved in a minimum amount of hot water, and an aqueous solution of trimethylamine hydrochloride (31.5 g, 0.33 mol) was added in excess, resulting in the formation of a yellow-white precipitate. The suspension was transferred to an ice bath and left resting for 30 minutes, filtered, and washed with cold water. The light yellow powder was then dried *in vacuo* at 90 °C, yielding 9.0 g (0.047 mol, 39% yield) of trimethylammonium *nido*-tetradecahydroundecaborane ($(CH_3)_3NHB_{11}H_{14}$).

$NaB_{11}H_{14}\cdot(C_6H_{14}O_3)_n$: ^1H NMR (D_2O, 400 MHz): δ (ppm) 0.30 – 2.60 (m, 11H, $B^{1-11}H$), 3.31 (s, 6H, OCH_3), 3.55 (m, 4H, CH_2) and 3.61 (m, 4H, CH_2). $^{11}B\{^1H\}$ NMR (D_2O, 128 MHz): δ (ppm) −17.3 ($B^{7-11}H$), −16.2 ($B^{2-6}H$) and −15.2 (B^1H). ^{11}B NMR (D_2O, 128 MHz): δ (ppm) −17.3 (d, $B^{7-11}H$, J = 145 Hz), −16.2 (d, $B^{2-6}H$, J = 145 Hz) and −15.1 (d, B^1H, J = 130 Hz).

$(CH_3)_3NHB_{11}H_{14}$: ^1H NMR (CD_3CN, 400 MHz): δ (ppm) 0.50 – 2.40 (m, 11H, $B^{1-11}H$), 2.73 (s, 9H, NCH_3). $^{11}B\{^1H\}$ NMR (CD_3CN, 128 MHz): δ (ppm) −16.8 ($B^{7-11}H$), −16.0 ($B^{2-6}H$) and −14.2 (B^1H). ^{11}B NMR (CD_3CN, 128 MHz): δ (ppm) −16.9 (d, $B^{7-11}H$, J = 120 Hz), −15.9 (d, $B^{2-6}H$, J = 120 Hz) and −14.2 (d, B^1H, J = 145 Hz).

Synthesis of alkali metal *nido*-tetradecahydroundecaborane, $MB_{11}H_{14}$ (*M* = Li, Na, K)

$$(CH_3)_3NHB_{11}H_{14(aq)} + 2MOH_{(aq)} \xrightarrow{H_2O,\ 100\ ^\circ C} M_2B_{11}H_{13(aq)} + (CH_3)_3N_{(g)} + 2H_2O_{(l)} \quad (3)$$

$$M_2B_{11}H_{13(aq)} + HCl_{(aq)} \xrightarrow{H_2O,\ 80\ ^\circ C} MB_{11}H_{14(aq)} + MCl_{(aq)} \quad (4)$$

$$M_2B_{11}H_{13(aq)} + H_2SO_{4(aq)} \xrightarrow{H_2O,\ 80\ ^\circ C} MB_{11}H_{14(aq)} + MHSO_{4(aq)} \quad (5)$$

The synthesis of $MB_{11}H_{14}$ (*M* = Li, Na, K) was adapted from a methodology presented by Klanberg and Muetterties.[28] In this report, they demonstrate a procedure to obtain $CsB_{11}H_{14}$ by initially synthesizing $Na_2B_{11}H_{13}$ (eq. 3) and show that the reduction of the pH of the reaction medium to 4-5 with addition of H_2SO_4 yields $NaB_{11}H_{14}$ (eq. 5). However, they do not demonstrate how to isolate $NaB_{11}H_{14}$, neither how to prepare $LiB_{11}H_{14}$ or $KB_{11}H_{14}$, which is presented here for the first time based on the following method.

Trimethylammonium *nido*-tetradecahydroundecaborane (1.5 g, 7.77 mmol for $LiB_{11}H_{14}$ and $NaB_{11}H_{14}$ and 0.5 g, 2.59 mmol for $KB_{11}H_{14}$) was dissolved in a 0.5 mol·L^{-1} aqueous solution of metal hydroxide (LiOH: 75 mL, NaOH: 75 mL, KOH: 30 mL) and heated to boiling (100 °C) for ~ 20 minutes (eq. 3). The solution was cooled to room temperature, filtered, and the filtrate was heated to 80 °C. The pH of the solution was adjusted to 4 – 5 by slow addition of 1.0 mol·L^{-1} aqueous solution of inorganic acid ($LiB_{11}H_{14}$ and $NaB_{11}H_{14}$ were prepared with HCl, eq. 4, and $KB_{11}H_{14}$ with H_2SO_4, eq. 5), and then washed with diethyl ether at room temperature. The organic layer, a yellowish liquid, was isolated from the aqueous solution, flushed with argon, and dried *in vacuo* at 80 °C, which resulted in the formation of a

deliquescent white powder of alkali metal *nido*-tetradecahydroundecaborane ($LiB_{11}H_{14}$: 0.89 g, 6.36 mmol, 82% yield, $NaB_{11}H_{14}$: 0.68 g, 4.36 mmol, 56% yield, $KB_{11}H_{14}$: 0.30g, 1.74 mmol, 67% yield).

$MB_{11}H_{14}$ (*M* = Li, Na and K): ^{1}H NMR (DMSO-d_6, 400 MHz): δ (ppm) −0.30 – 2.50 (m, 11H, B$^{1-11}$*H*). ^{11}B{^{1}H} NMR (DMSO-d_6, 128 MHz): δ (ppm) −16.8 (*B*$^{7-11}$H), −16.0 (*B*$^{2-6}$H) and −14.2 (*B*^{1}H). ^{11}B NMR (DMSO-d_6, 128 MHz): δ (ppm) −16.9 (d, *B*$^{7-11}$H, *J* = 125 Hz), −15.9 (d, *B*$^{2-6}$H, *J* = 125 Hz) and −14.2 (d, *B*^{1}H, *J* = 135 Hz).

Characterization

Nuclear Magnetic Resonance (NMR), Fourier Transformed Infrared Spectroscopy (FTIR), simultaneous Thermogravimetry (TGA) and Differential Scanning Calorimetry (DSC), Thermal Decomposition Analysis by Mass Spectrometry (TDA-MS), X-Ray Powder Diffraction (XRPD) and Electrochemical Impedance Spectroscopy (EIS) were applied for the characterization of all samples. Temperature Programmed Photographic Analysis (TPPA) was conducted with the sample of ball-milled (B.M.) $KB_{11}H_{14}$. Linear sweep voltammetry (LSV) measurements were performed for the samples of $LiB_{11}H_{14}\cdot(H_2O)_n$ and $NaB_{11}H_{14}\cdot(H_2O)_n$. The crystal structures of $LiB_{11}H_{14}\cdot 2H_2O$ and room temperature $KB_{11}H_{14}$ were determined by single-crystal X-ray diffraction data and synchrotron powder X-ray diffraction data, respectively. Density Functional Theory (DFT) calculations were performed for $B_{11}H_{14}^-$ and $B_{11}H_{13}OH^-$ to obtain structural information and theoretical NMR and FTIR data for both anions. Detailed information for all analyses can be found in the Electronic Supplementary Information.

RESULTS AND DISCUSSION

Sample Preparation and Characterization

The synthesis of $NaB_{11}H_{14}$ can be accomplished by different synthetic routes, as demonstrated by known reactions 6 and 7:[29,30]

$$NaBH_{4(s)} + B_{10}H_{14(l)} \xrightarrow{\text{dioxane, } 90\,^\circ\text{C}} NaB_{11}H_{14}\cdot(\text{dioxane})_{n(sol)} + 2H_{2(g)} \quad (6)$$

$$11B_5H_{9(g)} + 5NaH_{(sol)} \xrightarrow{\text{glyme, } 85\,^\circ\text{C}} 5NaB_{11}H_{14(sol)} + 17H_{2(g)} \quad (7)$$

The use of decaborane ($B_{10}H_{14}$) and pentaborane (B_5H_9) in chemical reactions is preferably avoided since they are highly toxic and potentially explosive. Moreover, they are expensive reactants, which make their use for the synthesis of $NaB_{11}H_{14}$ impractical in scale-up production. Hence, the reaction of 1-bromopentane with sodium borohydride in diglyme (eq. 1), first demonstrated by Dunks *et al.*,[26] becomes the safest and cheapest synthetic pathway for $B_{11}H_{14}^-$ salts. Here, a reaction mechanism is hypothesised in equations 8 – 11 and explained as follows.[26,31,32] The reduction of the alkyl halide by BH_4^- in diglyme produces diborane (B_2H_6), a highly reactive gas (eq. 8). Further reaction of this compound with the BH_4^- induces the formation of $B_3H_8^-$, a product of the thermal decomposition of $B_2H_7^-$ (eqs. 9 and 10). High yields of $B_3H_8^-$ are achieved when the reaction occurs at ~100 °C in an ethereal solvent, such as diglyme. $B_3H_8^-$ reacts with excess diborane and produces $NaB_{11}H_{14}$ in a dehydrocondensation step (eq. 11).[26,31,32] The overall reaction of this synthetic route is shown in equation 1.

$$10NaBH_4 + 10C_5H_{11}Br \rightarrow 5B_2H_6 + 10NaBr + 10C_5H_{12} \quad (8)$$

$$B_2H_6 + 2NaBH_4 \rightarrow 2NaB_2H_7 \quad (9)$$

$$2NaB_2H_7 \rightarrow NaB_3H_8 + NaBH_4 + H_2 \quad (10)$$

$$NaB_3H_8 + 4B_2H_6 \rightarrow NaB_{11}H_{14} + 9H_2 \quad (11)$$

The main drawback of the dehydrocondensation reaction (eq. 1) is the formation of $NaB_{11}H_{14}$ strongly coordinated with diglyme, and the presence of this coordinated solvent changes its properties as an ionic conductor (see section on 'Solid-State Ionic Conductivity'). One step that can be undertaken to remove diglyme from the salt is to substitute the sodium for a large monovalent cation, such as trimethylammonium, which yields a product that is water-insoluble, non-coordinating towards diglyme, and easily isolated (eq. 2).[27] ^{11}B NMR, FTIR, and XRPD data for $(CH_3)_3NHB_{11}H_{14}$ are summarised in Figs. S1 and S2. The reaction of $(CH_3)_3NHB_{11}H_{14}$ with a strong alkaline solution (pH 10 and above) of lithium hydroxide, sodium hydroxide, or potassium hydroxide, results in the deprotonation of $B_{11}H_{14}^-$ with consequent formation of $B_{11}H_{13}^{2-}$ (Fig. S3). The reaction is conducted at 100 °C in an open vessel to ensure that $(CH_3)_3NH^+$ is eliminated from the reaction mixture as trimethylamine, $(CH_3)_3N$ (boiling point 2.9 °C at 1 atm).[28] When the alkaline solution of $B_{11}H_{13}^{2-}$ is treated with an aqueous solution of an inorganic acid, such as H_2SO_4 or HCl, $B_{11}H_{13}^{2-}$ is progressively converted back to $B_{11}H_{14}^-$ and a side-product of boric acid ($B(OH)_3$). The resonances of $B_{11}H_{13}^{2-}$ in the ^{11}B NMR spectrum of the aqueous medium are no longer observed after reducing the pH of the reaction below 5.0 (Fig. S4). In order to isolate $B_{11}H_{14}^-$ from the reaction mixture that contains $B(OH)_3$, a liquid-liquid extraction of the aqueous solution at pH 4.5 was conducted with diethyl ether. The strong affinity of boric acid with water results in the majority of this compound remaining within the water layer, whereas diethyl ether extracts the majority of the *nido*-tetradecahydroundecaborane salt. An aliquot of the organic layer extracted from the aqueous solution containing $LiB_{11}H_{14}$ and $B(OH)_3$ was dissolved in DMSO-d_6 and analysed using ^{11}B NMR spectroscopy (Fig. S5). No resonance at 19.4 ppm from $B(OH)_3$ can be observed from the ethereal layer, which indicates that diethyl ether can be used as an extraction solvent for *nido*-undecaborane salt. Besides that, $B_{11}H_{14}^-$ cage undergoes hydrolysis when dried in aqueous solution, therefore the extraction of the salt with diethyl ether is fundamental to avoid such event. The organic layer was then isolated from the aqueous solution and purged with argon in order to eliminate any oxygen and avoid the formation of any oxidation product of $B_{11}H_{14}^-$. The solution was dried *in vacuo* at 80 °C, and for all the cations used, a white deliquescent powder was obtained, which was stored under argon. An analysis on the ^{11}B NMR spectrum of each compound after drying (Fig. 1) shows the presence of $B_{11}H_{14}^-$ represented by the resonances at δ = −14.2, −16.0 and −16.8 ppm. Additional resonances are also observed in the spectra of $LiB_{11}H_{14}$ and $NaB_{11}H_{14}$ (δ = 18.8, −9.6, −10.7, −23.3, −29.1, and −40.0 ppm) that represent the chemical shifts (observed and calculated, Table S10) of the hydroxo-*nido*-undecaborate $B_{11}H_{13}OH^-$,[33] which is formed as a side product. During synthesis, in which the aqueous solution is acidified in order to convert $B_{11}H_{13}^{2-}$ into $B_{11}H_{14}^-$, hydronium salts of $B_{11}H_{14}^-$

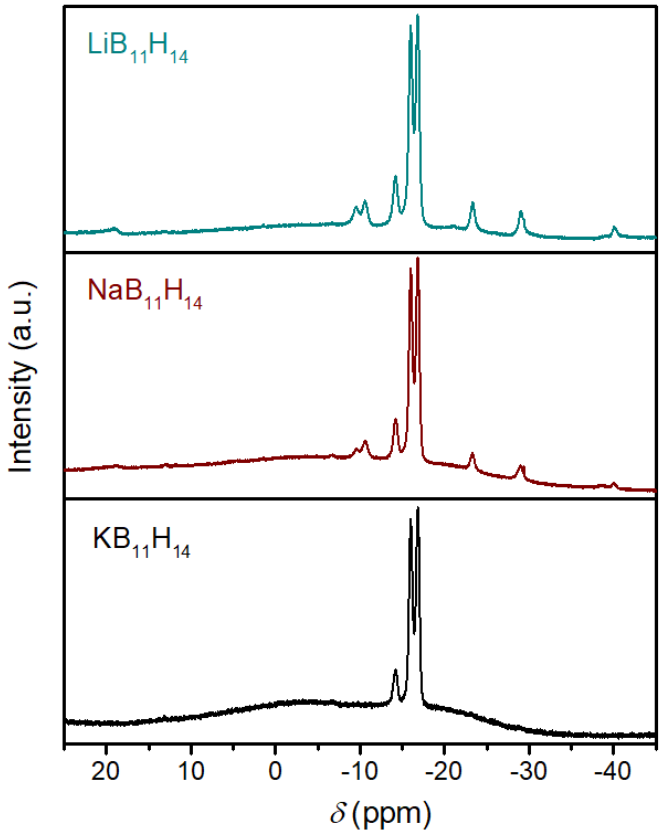

Fig. 1. $^{11}B\{^1H\}$ NMR spectra (128 MHz) of $LiB_{11}H_{14}$, $NaB_{11}H_{14}$, and $KB_{11}H_{14}$ in DMSO-d_6 (top to bottom), which show the presence of $B_{11}H_{14}^-$ anion in all spectra, observed at δ = −14.2, −16.0 and −16.8 ppm. The resonances at δ = 18.8, −9.6, −10.7, −23.3, −29.1, and −40.0 ppm observed in the spectra of $LiB_{11}H_{14}$ and $NaB_{11}H_{14}$ represent $B_{11}H_{13}OH^-$, which is formed as a by-product in the reaction.

may also be formed, which decompose into $B_{11}H_{13}OH^-$ during evaporation of the organic layer and drying of the powder. Similar reactions have previously been observed for hydronium salts of $B_{12}H_{12}^{2-}$ with hydrogen evolution and consequent formation of $B_{12}H_{11}OH^{2-}$, upon decreasing the water content or heating.[27] As Li^+ and Na^+ are small cations, they may compete with H_3O^+ for the formation of salts of $B_{11}H_{14}^-$, whereas large monovalent cations, such as K^+, $(CH_3)_3NH^+$, and Cs^+,[28] yield stable salts of $B_{11}H_{14}^-$, not allowing formation of the hydronium salt nor $B_{11}H_{13}OH^-$. Furthermore, the estimated ionic radius of 1.00 Å for H_3O^+ is similar to six-coordinate Na^+ (1.07 Å) and even greater than the six-coordinate Li^+ radius (0.79 Å),[34,35] which explains the formation of acids of $B_{11}H_{14}^-$ when small cations are used for the synthesis. The additional resonances are also observed in the ^{11}B NMR data of commercial $NaB_{11}H_{14}$,[25] however, they have previously been unidentified.

A more pure $B_{11}H_{14}^-$ compound of Li^+ or Na^+ can also be obtained if the liquid-liquid extraction step is applied for the aqueous solution at pH 7.5 (rather than 4.5), and dried under the same conditions (80 °C), as less hydronium ions are available in the medium. However, at neutral pH, $B_{11}H_{13}^{2-}$ remains present, which reduces the yield of the synthesis. This can only be accomplished since diethyl ether does not extract $B_{11}H_{13}^{2-}$ from the medium. Fig. S6 shows the $^{11}B\{^1H\}$ NMR spectra of $LiB_{11}H_{14}$ obtained after organic layer extractions at pH 4.5 and 7.5. Integration of the NMR resonances shows that the sample obtained from low pH has approximately 12 mol% of $B_{11}H_{13}OH^-$, whereas the sample that was obtained from neutral pH contains approximately 4 mol% of $B_{11}H_{13}OH^-$.

FTIR spectroscopy (Fig. S7) in conjunction with DFT calculated vibrational spectroscopy data (Fig. S8) confirms the presence of B–H bonds through the stretching mode at 2500 cm^{-1}.[36,37] There is also an absence of $(CH_3)_3NH^+$ represented by the lack of the bands at 3165 cm^{-1} and 970 cm^{-1}, which are assigned to the stretching modes of the ^+N–H and C–N^+ bonds, respectively (Fig. S1(B)).[38] The data reveal that water molecules are present in the cluster of the samples of Li and Na, represented by the bands at 3800 – 3200 cm^{-1} (O–H stretching) and 1610 cm^{-1} (H–O–H bending).[39] The absence of a H–O–H bending mode in the FTIR spectrum of $KB_{11}H_{14}$ proves that the cation is not solvated by water. As Li^+ and Na^+ have higher charge density than K^+, they coordinate more strongly to water and become strongly hydrated cations.[40]

The presence of water was also confirmed by MS analysis of the gases released from the as-synthesised boranes upon heating at high vacuum (Fig. S9). Samples of $LiB_{11}H_{14}$ and $NaB_{11}H_{14}$ lead to higher intensity peaks at m/z = 18 compared to the potassium version, which is in agreement with the FTIR data. MS data on all samples also show significant hydrogen evolution at temperatures above 200 °C, indicating their thermal decomposition (Fig. S10). This correlates well with TGA-DSC data (Figs. S11-S13), where a significant mass loss and a clear exothermic feature at ~210 °C are observed in all cases. Two steps of hydrogen evolution can be observed in the MS data for $LiB_{11}H_{14}$ (Fig. S10), one at ~165 °C, corresponding to the water release temperature (Fig. S9), and another one at ~220 °C, which is also observed in its DSC scan (Fig. S11). The MS data for $NaB_{11}H_{14}$ (Fig. S9) demonstrates that water is released upon heating before and at the decomposition temperature of 205 °C. The total mass loss upon decomposition of 3.9% and 4.3% for $LiB_{11}H_{14}$ and $NaB_{11}H_{14}$, respectively, is attributed to the release of water and hydrogen, whereas $KB_{11}H_{14}$ show a total mass loss of 2.9 wt%, which accounts for hydrogen evolution. Only $KB_{11}H_{14}$ undergoes a polymorphic phase transition, which is evident by an endothermic event at 140 °C, before it decomposes. DSC scans upon heating and cooling of pristine and ball-milled (B.M.) $KB_{11}H_{14}$ (Fig. 2) show endo- and exothermic features during thermal cycling, at ~140 and 75 °C respectively, which indicates a reversible phase transition. The reversibility obtained in pristine and ball-milled material indicates that the mechanical-induced modification does not stabilize the high temperature polymorph at room temperature, as can be seen in other ion conducting materials.[41,42]

Structural Characterization

XRPD patterns of $LiB_{11}H_{14}\cdot(H_2O)_n$, $NaB_{11}H_{14}\cdot(H_2O)_n$, and $KB_{11}H_{14}$ are illustrated in Fig. 3. As mentioned previously, the materials were dried at 80 °C *in vacuo* prior to analysis.

XRPD data has not previously been reported for $LiB_{11}H_{14}\cdot(H_2O)_n$ nor $KB_{11}H_{14}$. However, it appears as though the Li and Na analogues share a structural configuration due to similarities in the XRD pattern. The XRPD pattern of $NaB_{11}H_{14}\cdot(H_2O)_n$ appears

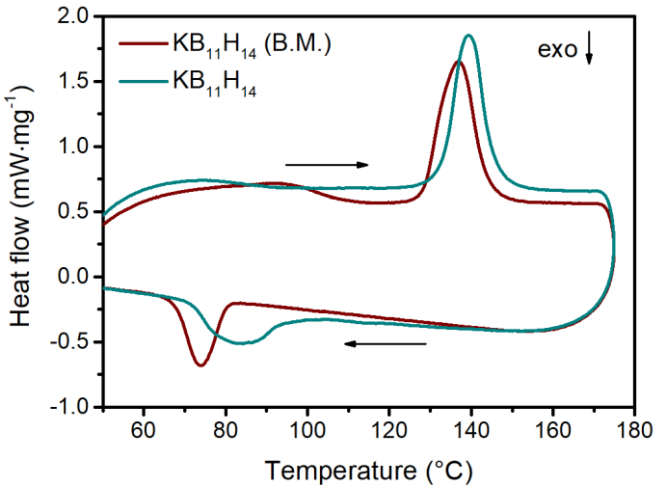

Fig. 2. DSC plots for pristine and ball-milled (B.M.) $KB_{11}H_{14}$ upon heating and cooling between 40 and 170 °C ($\Delta T/\Delta t$ = 10 °C·min^{-1}) under 40 mL·min^{-1} of argon flow.

similar to that presented by Tang *et al.*[21] for the sample '*a*-$NaB_{11}H_{14}$' that exhibits a face centred cubic polymorph ($Fm\bar{3}m$, a = 10.1520(19) Å) at room temperature. This also correlates well with our indexing, which suggests $Fm\bar{3}m$, a = 10.101(1) Å for $NaB_{11}H_{14}\cdot(H_2O)_n$ and $Fm\bar{3}m$, a = 10.0736(5) Å for $LiB_{11}H_{14}\cdot(H_2O)_n$. In contrast, the room temperature polymorph of $KB_{11}H_{14}$ (denoted α) was indexed in $P\bar{1}$ (see Tables S1-2 and Figures S14-15). However, a high temperature polymorphic structural transition is observed at 135 °C, in agreement with DSC data and *in-situ* XRPD data (see Figure S16). The high temperature $KB_{11}H_{14}$ polymorph (denoted β) was indexed in $Fm\bar{3}m$, a = 10.19473(4) Å, matching the structure type seen at room temperature for the lighter alkali metal-$B_{11}H_{14}$ compounds. The cubic space groups are reminiscent of the highly dynamic structures observed in the class of metal boron-hydrogen salts, where the anion undergoes significant reorientational motion and cannot be easily defined in the crystal structure.[43] The unit cell and structure of α-$KB_{11}H_{14}$ differs greatly to that of the hydrated $NaB_{11}H_{14}$ and $LiB_{11}H_{14}$ moieties. As can be seen from Fig. S15, the $KB_{11}H_{14}$ packing structure, when viewed along the a and b axis consists of separate columns of K atoms and $B_{11}H_{14}^-$ anions. The distances between K atoms through the columns along the a and b axis are ~7.1 Å, whereas the shortest K–K distances are 5.278(5) Å. To determine the accurate hydrogen positions, neutron diffraction would be required, especially due to the dynamic nature of these anions and the bridging hydrogens at the apex of the $B_{11}H_{14}^-$ moieties.

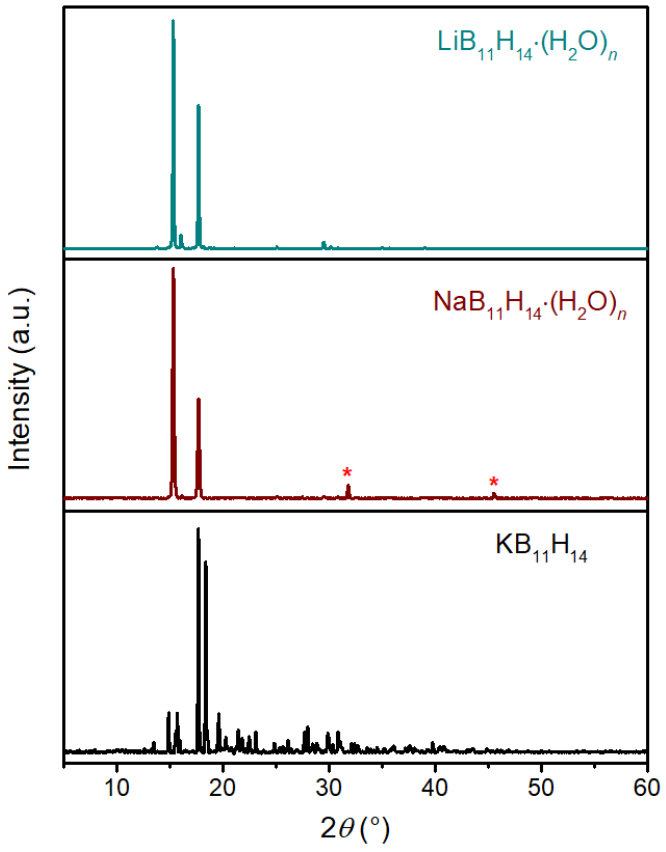

Fig. 3. XRPD pattern for $LiB_{11}H_{14}\cdot(H_2O)_n$, $NaB_{11}H_{14}\cdot(H_2O)_n$, and $KB_{11}H_{14}$ at room temperature. λ = 1.54056 Å. Asterisks at 2Θ = 31.8° and 45.5° in the $NaB_{11}H_{14}\cdot(H_2O)_n$ pattern represent inadvertent NaCl contamination.

Due to the high ionic conductivity of $NaB_{11}H_{14}\cdot(H_2O)_n$ at room temperature, electrochemical impedance spectroscopy data of this sample was also collected at low temperatures, and the lowest conductance activity was achieved at –40 °C (5.0 x 10^{-6} S·cm^{-1}). AC impedance measurements were also performed at –70 °C, but no activity was observed at this temperature. Below –40 °C, it is hypothesised that a sudden decrease in conductivity could arise from a polymorphic phase transition upon cooling to a less symmetric crystal structure. In order to investigate this, the diffraction pattern for $NaB_{11}H_{14}\cdot(H_2O)_n$ was acquired at –100 °C, with the data showing that the material undergoes a reversible polymorphic transition at low temperature by the emergence of additional Bragg reflections in the diffraction pattern. The $NaB_{11}H_{14}\cdot(H_2O)_n$ spontaneously returns to its original polymorph upon natural heating to room temperature (Fig. 4). This discovery raises the question as to whether the room temperature $NaB_{11}H_{14}\cdot(H_2O)_n$ crystal structure (and the Li analogue) is actually a 'high-temperature' polymorph that displays reorientational dynamics, akin to other metal boron-hydrogen compounds.[20,22] This may be indicated by the symmetric cubic structure-type, but further investigations into its crystal structure are required, perhaps utilising neutron diffraction.

Crystals of *nido*-tetradecahydroundecaboranes are often difficult to grow due to their extreme deliquescence. As the crystal of $LiB_{11}H_{14}\cdot2H_2O$ was grown without any application of heating / drying, its diffraction pattern, and thus structure and water content, differ from the sample that was used to investigate ionic conductivity. The presence of water in its crystal structure demonstrates that Li^+ favourably coordinates with water, even after the compound being extracted with an organic solution. The crystal structure of $LiB_{11}H_{14}\cdot2H_2O$ was solved in space group $C2/c$ with lattice parameters a = 10.4298(4) Å, b = 10.1040(2) Å, c = 42.3413(16) Å, β = 91.236(4)°, and V/Z = 557.62(9) Å^3 (Fig. S17, Table S1 & S3). Here, the Li-ions are in a pseudo-tetrahedral environment, with each Li-bound to three water molecules, with the fourth contact formed between a H-atom bound to the $B_{11}H_{14}^-$ anion. The Li–Li distances are between 2.86(1) and 2.891(7) Å. Two of the bound

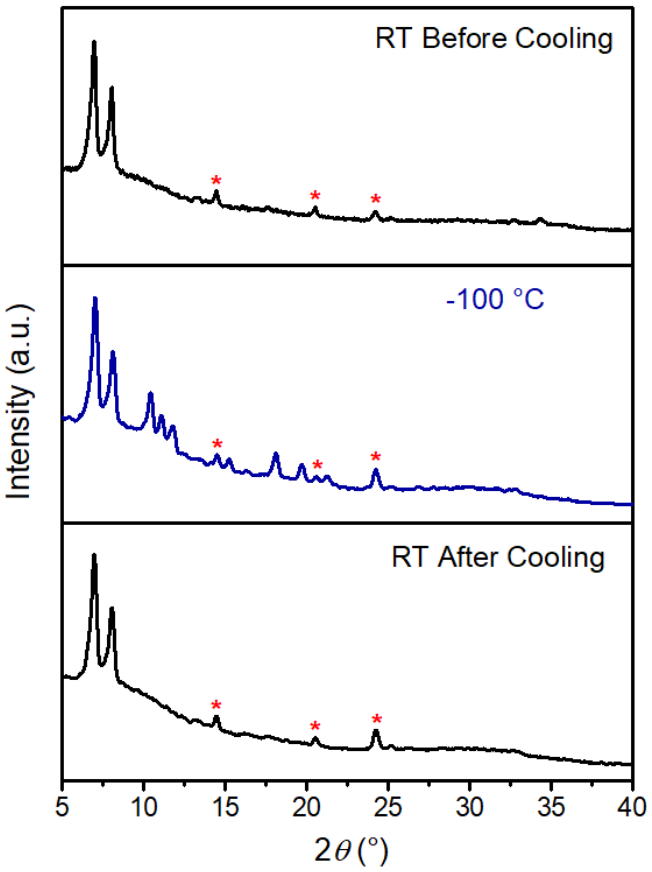

Fig. 4. XRPD pattern for $NaB_{11}H_{14}\cdot(H_2O)_n$ at room temperature (top), at −100 °C (centre) and at room temperature after natural heating (bottom). The sample was mounted in a capillary under argon atmosphere and measured with a Mo K_α source (λ = 0.7093 Å). Asterisks at 14.5°, 20.5° and 24.2° represent inadvertent NaCl contamination.

water molecules bridge between two separate Li-ions, forming a dimer (see Fig. S17), giving $Li^+(B_{11}H_{14})^-\cdot 2H_2O$ stoichiometrically, but forming $Li_2(B_{11}H_{14})_2\cdot 4H_2O$ units in the solid-state. In the crystal structure, two half-molecules are in the asymmetric unit, resulting in two symmetry independent $Li_2(B_{11}H_{14})_2\cdot 4H_2O$ units, though no difference in the connectivity or structure could be seen here. After drying, the material exhibits a face centred cubic structure (Fig. 3) with less than 2 water molecules in the unit $LiB_{11}H_{14}\cdot(H_2O)_n$ (n < 2).

Solid-State Ionic Conductivity

The solid-state ionic conductivity of $MB_{11}H_{14}\cdot(H_2O)_n$ (M = Li or Na) and $KB_{11}H_{14}$ before and after ball-milling (B.M.), along with $NaB_{11}H_{14}\cdot(C_6H_{14}O_3)_n$, was assessed as a function of temperature as illustrated in Fig. 5. The liquid-state ionic conductivity of the widely-used ionic liquid electrolyte, 1 mol·L^{-1} solution of 1-ethyl-3-methylimidazolium tetrafluoroborate ($EMIBF_4$) with lithium tetrafluoroborate ($LiBF_4$),[44] is displayed for comparison. The activation energy of ionic conductivity was calculated based on the Arrhenius plot (Fig. 5) for each compound by:

$$ln\ \sigma_{ion} = ln\ \sigma_o - \left(\frac{E_\sigma}{K_B}\right)\frac{1}{T} \qquad (12)$$

where σ_o is a pre-exponential factor (S·cm^{-1}), E_σ the activation energy (J), K_B the Boltzmann constant (1.3806 x 10^{-23} J·K^{-1}), and T the temperature (K).[45] The activation energy was calculated based on the slope of the plot of each material from 25 to 75 °C,

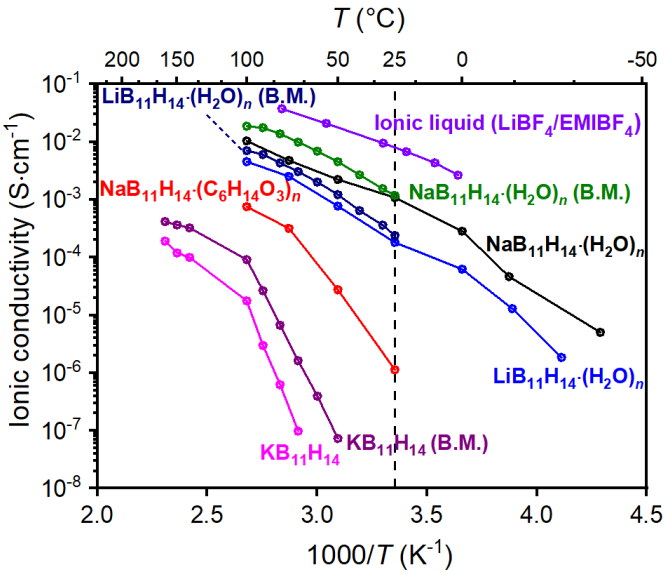

Fig. 5. Solid-state ionic conductivity of $NaB_{11}H_{14}\cdot(C_6H_{14}O_3)_n$, $LiB_{11}H_{14}\cdot(H_2O)_n$ (before and after B.M.), $NaB_{11}H_{14}\cdot(H_2O)_n$ (before and after B.M.), $KB_{11}H_{14}$ (before and after B.M.), and $LiBF_4/EMIBF_4$.[44]

except $KB_{11}H_{14}$ (before and after B.M.), which was measured from 70 to 100 °C. Nyquist plots of $LiB_{11}H_{14}\cdot(H_2O)_n$, $NaB_{11}H_{14}\cdot(H_2O)_n$, and $KB_{11}H_{14}$ at different temperatures are shown in Figs. S18 and S19.

The size of the cation plays an important role in the ionic conductivity of the material. Due to the large radius of K^+ (six-coordinate K^+, 1.38 Å),[35] the sample of $KB_{11}H_{14}$ shows a large activation energy (1.9 eV) that can only be significantly overcome at elevated temperature. Ball-milling the $KB_{11}H_{14}$ sample reduces its activation energy to 1.5 eV, and therefore, increases its ionic conductivity by approximately one order of magnitude. Despite the unusually high activation energy compared to other potassium boron-hydrogen materials, such as KB_3H_8 (E_σ = 0.44 eV),[46] $K_3(BH_4)(B_{12}H_{12})$ (E_σ = 0.37 eV)[46,47] and $KCB_{11}H_{12}$ (E_σ = 0.82 eV),[48] the K^+ conductivity in the pristine $KB_{11}H_{14}$ reaches an ionic conductivity of 1.2 x 10^{-4} S·cm^{-1} at 150 °C, whereas KB_3H_8 and $K_3(BH_4)(B_{12}H_{12})$ exhibit a K^+ conductivity in the order of 10^{-7} and 10^{-6}, respectively, at the same temperature.[46,47] The metal carborane, $KCB_{11}H_{12}$, in its ordered structure exhibits similar results of ionic conductivity when compared to the ball-milled sample of $KB_{11}H_{14}$, especially at 80 °C (~9.5 x 10^{-6} S·cm^{-1} and 6.7 x 10^{-6} S·cm^{-1}, respectively). Nevertheless, the high temperature polymorph that the metal carborane assumes presents an ionic conductivity about one order of magnitude higher than ball-milled $KB_{11}H_{14}$. The hysteretic conductivity behaviour observed for $KB_{11}H_{14}$ above 100 °C is a consequence of the polymorphic phase transition that the material undergoes, indicated by the DSC plot (Fig. 2) and *in-situ* XRPD data (Fig. S16), as discussed in the 'Structural Characterization' section. The potassium *nido*-borane sample assumes a disordered crystallographic structure at high temperature, which enhances its ionic conductivity, as observed for other metal boron-hydrogen materials.[20,22,48]

Temperature Programmed Photographic Analysis (Fig. S20) of $KB_{11}H_{14}$ was performed in order to check the condition of the pellet upon heating. The result reveals a slight volume

expansion at ~120-140 °C, which is related to the reversible polymorphic structural transition (Fig. 2 and S16). The pellet was heated up to 170 °C with no melting or release of solvent observed. Due to the volume change that the pellet undergoes upon heating, the data points between 110 and 130 °C were omitted from the ionic conductivity plot (Fig. 5) of pristine and ball-milled $KB_{11}H_{14}$, as they represent artefacts of the measurement (full data set is presented in Fig. S21).

Mechanical-induced modification is known to improve the cationic conductivity of other metal boron-hydrogen compounds, such as $LiBH_4$,[41] $Li_2B_{12}H_{12}$,[42] and $Na_2B_{12}H_{12}$[49] that had their ionic conductivity enhanced by at least two orders of magnitude when measured at the same temperature. Ball-milling may induce defects (cation or even hydrogen vacancies),[42,50] reduction of the crystallite size, and/or stabilization of a potential disordered high-temperature superionic polymorph, which are all factors that boost the ionic conductivity of a material.[49] However, ball-milling did not show significant improvement in the ionic conductivity of $NaB_{11}H_{14}\cdot(H_2O)_n$ and $LiB_{11}H_{14}\cdot(H_2O)_n$. Besides that, the activation energy of pristine $LiB_{11}H_{14}\cdot(H_2O)_n$ (0.5 eV) has not considerably changed upon ball-milling (0.5 eV), whereas $NaB_{11}H_{14}\cdot(H_2O)_n$ presented a small increase in its activation energy from 0.3 to 0.4 eV after ball-milling, but this is within the experimental uncertainty (±0.1 eV). Even though Li^+ (six-coordinate Li^+, 0.79 Å)[35] has an ionic radius smaller than Na^+ (six-coordinate Na^+, 1.07 Å),[35] $LiB_{11}H_{14}\cdot(H_2O)_n$ requires more energy to promote Li^+ migration and has lower ionic conductivity than $NaB_{11}H_{14}\cdot(H_2O)_n$. The differences in activation energy could be explained by the coordinated water, which is more strongly bound to the more charge-dense Li^+.

The presence of a coordinated solvent to the cation also shows an important contribution to the conductivity properties of the material, as reported by Møller *et al.*[51] As shown in (Fig. 5), $NaB_{11}H_{14}$ experiences a dramatic increase in cationic conductivity when replacing diglyme with water. $NaB_{11}H_{14}\cdot(C_6H_{14}O_3)_n$ has a high activation energy of 1.0 eV and an ion conductivity of 1.1 x 10^{-6} S·cm^{-1} at 25 °C, whereas $NaB_{11}H_{14}\cdot(H_2O)_n$ at the same temperature shows an outstanding result of 1.1 x 10^{-3} S·cm^{-1} and activation energy of 0.3 eV.

Diglyme molecules easily chelate with small cations, such as Na^+, due to the presence of ether-type oxygen atoms. These molecules solvate the metal and usually behave like crown glymes,[52] which may inhibit the cation displacement in the crystal structure. Small solvent molecules, like tetrahydrofuran (THF) and acetonitrile, have already been reported to assist the cationic diffusion through the crystal structure of $Li_2B_{12}H_{12}$.[51] The coordination of $LiBH_4$ with ammonia also increases its ionic conductivity, and it is proposed that NH_3 facilitates the migration of Li^+ through the lattice of $LiBH_4\cdot 1/2NH_3$.[53] In a similar way, water molecules coordinated to Na^+ may assist the diffusion of the cation through the crystal structure of $NaB_{11}H_{14}\cdot(H_2O)_n$ and contribute to its higher ionic conductivity and lower activation energy when compared to $NaB_{11}H_{14}\cdot(C_6H_{14}O_3)$.

Even though the presence of diglyme interferes with the ion conductivity, $NaB_{11}H_{14}\cdot(C_6H_{14}O_3)_n$ still exhibits higher ionic conductivities from 25 to 100 °C than other metal boron-hydrogen compounds, such as $Na_2B_{10}H_{10}$[54] and $Na_2B_{12}H_{12}$,[22] as shown in Fig. 6. Additionally, $NaB_{11}H_{14}\cdot(H_2O)_n$ exhibits considerably good cationic conductivity even at low temperatures, such as −40 °C (5.0 x 10^{-6} S.cm^{-1}), as well as $LiB_{11}H_{14}\cdot(H_2O)_n$, which shows an ionic conductivity of 1.8 x 10^{-6} S·cm^{-1} at −30 °C. The feature of reasonable solid-state ionic conductivities at sub-zero temperatures is vital for battery operation in cold climates.

Ball-milled $LiB_{11}H_{14}\cdot(H_2O)_n$ and $NaB_{11}H_{14}\cdot(H_2O)_n$ exhibit a lithium and sodium conductivity of 2.4 x 10^{-4} S·cm^{-1} and 1.2 x 10^{-3}

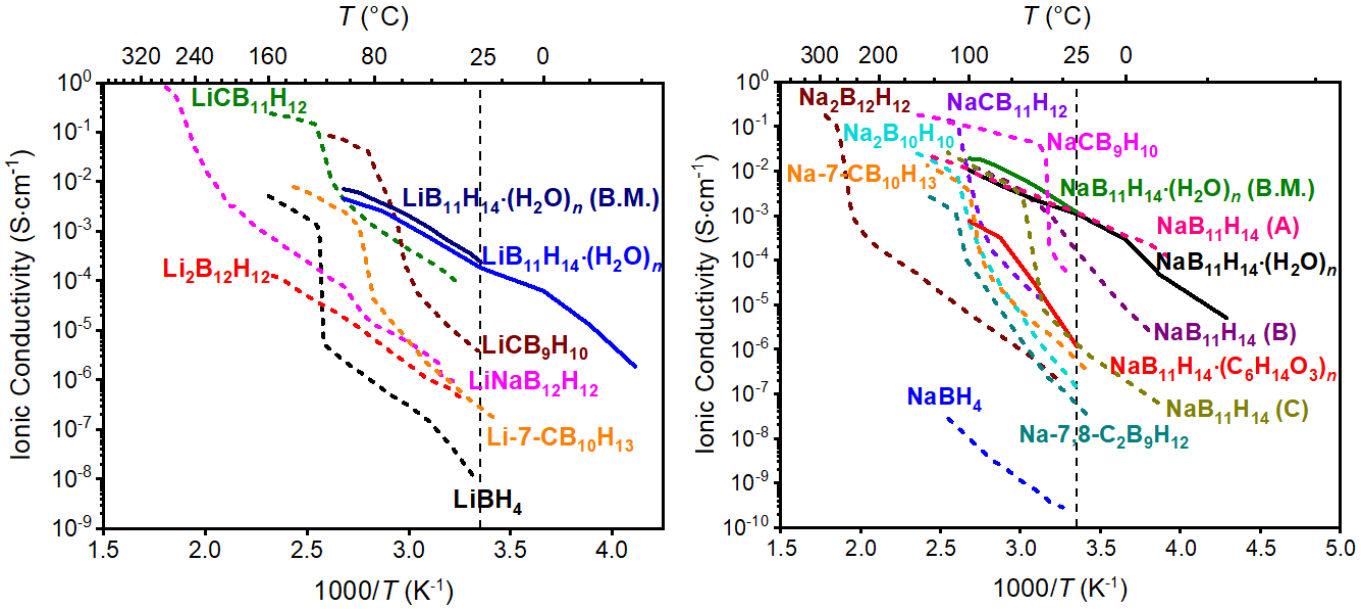

Fig. 6. Arrhenius plots of ionic conductivities of $LiB_{11}H_{14}\cdot(H_2O)_n$, $NaB_{11}H_{14}\cdot(H_2O)_n$, and $NaB_{11}H_{14}\cdot(C_6H_{14}O_3)_n$ compared with other Li (left) and Na (right) single anion boron-hydrogen materials: $LiCB_{11}H_{12}$,[62] $LiCB_9H_{10}$,[9] $LiBH_4$,[22] $Li_2B_{12}H_{12}$,[63] $LiNaB_{12}H_{12}$,[64] Li-7-$CB_{10}H_{13}$,[21] $NaCB_{11}H_{12}$,[62] $Na_2B_{12}H_{12}$,[22] $Na_2B_{10}H_{10}$,[54] $NaBH_4$,[54] Na-7-$CB_{10}H_{13}$,[21] Na-7,8-$C_2B_9H_{12}$,[21] $NaCB_9H_{10}$.[20] $NaB_{11}H_{14}$ (A) and (C) are the commercial version of $NaB_{11}H_{14}$ that were obtained from two different batches,[21] and (B) is a sample of $NaB_{11}H_{14}$ that was synthesised using decaborane.[25] The solid lines represent the ionic conductivity of the materials synthesised in this work.

S·cm⁻1, respectively, at 25 °C. To the author's knowledge, these results represent some of the highest Li^+ and Na^+ conductivities reported at room temperature for a metal boron-hydrogen compound (Fig. 6 and S22). Additionally, they exhibit superionic conductivity upon heating, with Li^+, and Na^+ conductivities of 7.1 x 10^{-3} S·cm^{-1} and 1.9 x 10^{-2} S·cm^{-1} at 100 °C for ball-milled $LiB_{11}H_{14}\cdot(H_2O)_n$ and $NaB_{11}H_{14}\cdot(H_2O)_n$, respectively.

$LiB_{11}H_{14}\cdot(H_2O)_n$ and $NaB_{11}H_{14}\cdot(H_2O)_n$ also exhibit higher ionic conductivity than other *nido*-anions, such as 7-$CB_{10}H_{13}^-$ and 7,8-$C_2B_9H_{12}^-$,[21] in the temperature range used in this study (Fig. 6). The incorporation of carbon to the *nido*-anion structure increases the charge polarization, and thus reduces its ionic conductivity.[21]

The $NaB_{11}H_{14}\cdot(H_2O)_n$ sample prepared in the present study exhibits the same crystal structure as a commercial sample in a previous study reported as '*a*-$NaB_{11}H_{14}$',[21] here denoted as $NaB_{11}H_{14}$ (A). The DSC (Fig. S12) and ionic conductivity results we obtain for $NaB_{11}H_{14}\cdot(H_2O)_n$ also match those for $NaB_{11}H_{14}$ (A) (Fig. 6). It is also clear that the ionic conductivity for $NaB_{11}H_{14}\cdot(H_2O)_n$ and $NaB_{11}H_{14}$ (A) is far superior to samples prepared in an alternative manner, $NaB_{11}H_{14}$ (B) and $NaB_{11}H_{14}$ (C). $NaB_{11}H_{14}$ (B) is a sample of $NaB_{11}H_{14}$ that was synthesised using decaborane in a previous work,[25] and $NaB_{11}H_{14}$ (C) is another commercial version of $NaB_{11}H_{14}$.[21] Both present an orthorhombic crystal structure, which differs completely from the *fcc* polymorph that $NaB_{11}H_{14}\cdot(H_2O)_n$ and $NaB_{11}H_{14}$ (A) exhibit. It may be that the previously reported "minor unknown impurities"[21] in $NaB_{11}H_{14}$ (A) are associated with coordinated water. Perhaps the presence of water molecules in the crystal structure stabilize its *fcc* disordered polymorph, and are responsible for the high ionic conductivity at room temperature (1.1 x 10^{-3} S·cm^{-1}).

Many solid-state electrolytes, including metal boron-hydrogen materials, may not present a wide electrochemical stability against Li or Na metal anodes.[55] For instance, $NaBH_4$ and $LiBH_4$ are stable up to ~2.0 V,[10,55] whereas $Na_2B_{12}H_{12}$ and $Li_2B_{12}H_{12}$ decompose at ~3.4 V.[10,55] It was also reported that $NaB_{11}H_{14}$ oxidizes at 2.6 V, and it exhibits a thermodynamic electrochemical window from 0.15 to 2.6 V vs Na/Na^+.[25] Therefore, in order to investigate the oxidative stability of $LiB_{11}H_{14}\cdot(H_2O)_n$ and $NaB_{11}H_{14}\cdot(H_2O)_n$, a linear sweep voltammetry experiment as proposed by Asakura *et al*.[56] was performed.

Fig. S23 shows the linear sweep voltammograms of the electrolytes tested. $NaB_{11}H_{14}\cdot(H_2O)_n$ exhibits an oxidative stability limit at 2.6 V, which is the same as previously reported for $NaB_{11}H_{14}$.[25] $LiB_{11}H_{14}\cdot(H_2O)_n$ demonstrated the first oxidation step at 2.1 V vs. Li/Li^+, which might be associated to residual water,[57] and a second step with high oxidative current at 2.9 V. The second linear sweep voltammogram cycle data for both materials do not demonstrate any oxidative current peaks, which indicates the irreversibility of the oxidation reaction.[17]

Interestingly, no observed changes are noted in the XRD patterns of $LiB_{11}H_{14}\cdot(H_2O)_n$ and $NaB_{11}H_{14}\cdot(H_2O)_n$ (Fig. S24) after the second cycle of LSV. This implies a bulk stability of both *nido*-boranes against Li and Na metal, respectively.[58] Nevertheless, oxidation of the sample can form an oxidised interphase between the electrolyte and the electrode, and depending on its properties, the performance of an ASSB can be greatly affected.[17] Discovering the properties of the created interphase, which also depends on the chosen cathode, is important for the development of an effective ASSB and requires future study.

The high ionic conductivity exhibited by $LiB_{11}H_{14}\cdot(H_2O)_n$ and $NaB_{11}H_{14}\cdot(H_2O)_n$ and their stability against Li and Na metal anodes, respectively, means that both materials become promising candidates to be used to form new mixed-anion boranes as solid-state electrolytes. Fig. S22 shows the Arrhenius plots of the ionic conductivities of some mixed-anion metal boron-hydrogen materials compared to $LiB_{11}H_{14}\cdot(H_2O)_n$ and $NaB_{11}H_{14}\cdot(H_2O)_n$. As previously reported,[9] the 0.7Li(CB_9H_{10})-0.3Li($CB_{11}H_{12}$) mixed-anion system exhibits superionic conductivity at room temperature, 6.7 × 10^{-3} S·cm^{-1} (Fig. S22), however, this material is formed by a mixture of two metal carboranes that present lower Li^+ conductivity than $LiB_{11}H_{14}\cdot(H_2O)_n$ at room temperature (Fig. 6) and higher cost. $Na_2(CB_9H_{10})(CB_{11}H_{12})$[59] and $Na_4C(B_{11}H_{12})_2(B_{12}H_{12})$[57] are also formed by a mixture of metal boranes that individually exhibit lower ionic conductivity at 25 °C (Fig. 6) and higher cost than $NaB_{11}H_{14}\cdot(H_2O)_n$. The hydrated sodium *nido*-borane even presents higher ionic conductivity than other mixed-anion compounds, such as $Na_4(B_{12}H_{12})(B_{10}H_{10})$[60] and $Na_3(BH_4)(B_{12}H_{12})$[61] (Fig. S22).

It should be noted that the presence of solvated water in the as-synthesised $NaB_{11}H_{14}\cdot(H_2O)_n$ confirmed by FTIR, TDA-MS, and TGA-DSC data has not previously been identified by researchers in their $NaB_{11}H_{14}$ samples.[21,25] Second, inconsistencies are reported between different batches of commercial $NaB_{11}H_{14}$,[21] which raises doubts on their exact stoichiometry or purity. In previous research,[25] heating $NaB_{11}H_{14}$ above 100 °C, results in a significant formation (~50% from NMR) of, what is identified here as, $B_{11}H_{13}OH^-$. Based on our investigation of the synthesis, this by-product is only formed if the powder contains acidic hydronium (H_3O^+) cations, akin to previous research on $B_{10}H_{10}^{2-}$ and $B_{12}H_{12}^-$.[27] Possibly, the reported $NaB_{11}H_{14}$ ionic conductivity studies had solid-solutions, solvates, or multi-phase compounds, which would explain the differences observed between the many different crystallographic polymorphs or phases present.[21,25] Despite this, the measured ionic conductivities of $NaB_{11}H_{14}$ are, in most cases, similar.

Conclusions

An optimised low cost procedure for the preparation of $MB_{11}H_{14}\cdot(H_2O)_n$ (*M* = Li and Na), and $KB_{11}H_{14}$ and a proposed reaction mechanism are presented. This comprehensive study fills a gap in the literature, which has unexplained differences between $NaB_{11}H_{14}$ samples depending on their origin or synthetic method. The use of diethyl ether to extract *nido*-borane salts from the aqueous medium is an important finding in order to avoid hydrolysis of the cage and to isolate it from boric acid. Of great importance is also the discovery that acidification of the $B_{11}H_{13}^{2-}$, precursor during synthesis, can also form the hydronium salt of $B_{11}H_{14}^-$, i.e. $(H_3O)B_{11}H_{14}$. The

hydronium salt reacts upon heating / drying and releases hydrogen to form $B_{11}H_{13}OH^-$ as a side product. This important finding may explain some of the differing literature results on $NaB_{11}H_{14}$. The hydronium salt formation is more prevalent with smaller cations as $KB_{11}H_{14}$ is formed without this impurity. The presence of solvated water in powders of $LiB_{11}H_{14}$ and $NaB_{11}H_{14}$ is confirmed by FTIR, TDA-MS, and TGA-DSC, whereas $KB_{11}H_{14}$ is anhydrous, likely due to its larger radius and thus lower charge density, making it less coordinating towards this molecule. All $MB_{11}H_{14}$ compounds decompose at ~210 °C with release of hydrogen. Additionally, $KB_{11}H_{14}$ undergoes a reversible polymorphic phase transition upon heating / cooling between 40 and 170 °C. The room temperature crystal structure of $KB_{11}H_{14}$ was solved in space group $P\overline{1}$ and assume a high temperature face centred cubic polymorph ($Fm\overline{3}m$) exhibiting increased ionic conductivity results. The crystal structure of $LiB_{11}H_{14}{\cdot}2H_2O$ was indexed in $C2/c$, and upon dehydration, $LiB_{11}H_{14}{\cdot}(H_2O)_n$ ($n < 2$) exhibits a face centred cubic polymorph, which matches with the structure type seen for $NaB_{11}H_{14}{\cdot}(H_2O)_n$ at room temperature and β-$KB_{11}H_{14}$ polymorph. This suggests that the high ionic conductivity observed for those samples may be related to the dynamics in the cubic crystal structure they exhibit.

$LiB_{11}H_{14}{\cdot}(H_2O)_n$ and $NaB_{11}H_{14}{\cdot}(H_2O)_n$ feature promising ionic conductivity at room temperature, 1.8×10^{-4} S·cm^{-1} and 1.1×10^{-3} S·cm^{-1}, respectively, and even show conductivity at sub-zero temperatures, such as −30 °C. These outstanding results may be related to as-yet-unknown reorientational dynamics within the crystal structure or due to the fact that the cation is solvated with water, which may facilitate the migration of the cation through the crystal structure. Moreover, the oxidative stability limit of $LiB_{11}H_{14}{\cdot}(H_2O)_n$ and $NaB_{11}H_{14}{\cdot}(H_2O)_n$ were identified as 2.1 V vs. Li^+/Li and 2.6 V vs. Na^+/Na, respectively.

$LiB_{11}H_{14}{\cdot}(H_2O)_n$ and $NaB_{11}H_{14}{\cdot}(H_2O)_n$ are considered some of the best metal boron-hydrogen ion conductors within the respective cation compound class. Besides that, the safe and low-cost synthesis method enables these materials to be produced on a scale for practical applications. Finally, the synthesised compounds may act as precursors in future work to prepare mixed-anion compounds with even higher ionic conductivities. The results show great promise towards the development of a solid-state electrolyte, and eventually ASSBs, however further battery studies involving these electrolytes need to be undertaken.

Conflicts of interest

There are no conflicts to declare.

Acknowledgements

DHPS acknowledges the support from Curtin-ATN South American Scholarship and Tuition Fee-Offset Scholarship through Curtin University. MP and SAM thank the Australian Research Council (ARC) for a Future Fellowship (FT160100303) (FT200100243). KTM thanks The Independent Research Fund Denmark for International Postdoctoral Grant 8028-00009B and The Carlsberg Foundation for Reintegration Fellowship CF19-0465. CEB, MP, TDH, and KTM acknowledge the financial support of the Global Innovation Linkage (GIL73589). CEB acknowledges the financial support of the ARC for the LIEF grant LE170100199. SAM gratefully acknowledges the facilities, and the scientific and technical assistance of Microscopy Australian at the Centre for Microscopy, Characterisation & Analysis, The University of Western Australia, a facility funded by the University, State and Commonwealth Governments. This research was undertaken on the Powder Diffraction beamline at the Australian Synchrotron, part of ANSTO.

References

1 B. R. S. Hansen, M. Paskevicius, M. Jørgensen and T. R. Jensen, *Chem. Mater.*, 2017, **29**, 3423–3430.
2 B. C. Liu, F. Li, L. Ma and H. Cheng, *Adv. Mater.*, 2010, **22**, E28–E62.
3 H. Chen, T. Ngoc Cong, W. Yang, C. Tan, Y. Li and Y. Ding, *Prog. Nat. Sci.*, 2009, **19**, 291–312.
4 A. Mauger, C. M. Julien, A. Paolella, M. Armand and K. Zaghib, *Materials (Basel).*, 2019, **12**, 3892.
5 J. C. Bachman, S. Muy, A. Grimaud, H. Chang, N. Pour, S. F. Lux, O. Paschos, F. Maglia, S. Lupart, P. Lamp, L. Giordano and Y. Shao-Horn, *Chem. Rev.*, 2016, **116**, 140–162.
6 A. Gigante, L. Duchene, R. Moury, M. Pupier, A. Remhof and H. Hagemann, *ChemSusChem*, 2019, **12**, 4832–4837.
7 F. Zheng, M. Kotobuki, S. Song, M. O. Lai and L. Lu, *J. Power Sources*, 2018, **389**, 198–213.
8 M. Ue and K. Uosaki, *Curr. Opin. Electrochem.*, 2019, **17**, 106–113.
9 S. Kim, H. Oguchi, N. Toyama, T. Sato, S. Takagi, T. Otomo, D. Arunkumar, N. Kuwata, J. Kawamura and S. Orimo, *Nat. Commun.*, 2019, **10**, 1–9.
10 Z. Lu and F. Ciucci, *Chem. Mater.*, 2017, **29**, 9308–9319.
11 S. B. Aziz, T. J. Woo, M. F. Z. Kadir and H. M. Ahmed, *J. Sci. Adv. Mater. Devices*, 2018, **3**, 1–17.
12 T. Yang, J. Zheng, Q. Cheng, Y. Hu and C. K. Chan, *ACS Appl. Mater. Interfaces*, 2017, **9**, 21773–21780.
13 Y. Ren, K. Chen, R. Chen, T. Liu, Y. Zhang and C. Nan, *J. Am. Ceram. Soc.*, 2015, **98**, 3603–3623.
14 V. Thangadurai, S. Narayanan and D. Pinzaru, *Chem. Soc. Rev*, 2014, **43**, 4714–4727.
15 Z. Jiang, T. Liang, Y. Liu, S. Zhang, Z. Li, D. Wang, X. Wang, X. Xia, C. Gu and J. Tu, *ACS Appl. Mater. Interfaces*, 2020, **12**, 54662–54670.
16 H. Pan, Z. Cheng, P. He and H. Zhou, *Energy and Fuels*, 2020, **34**, 11942–11961.
17 F. Han, Y. Zhu, X. He, Y. Mo and C. Wang, *Adv. Energy Mater.*, 2016, **6**, 1501590.
18 B. R. S. Hansen, M. Paskevicius, H. Li, E. Akiba and T. R. Jensen, *Coord. Chem. Rev.*, 2016, **323**, 60–70.
19 M. Paskevicius, L. H. Jepsen, P. Schouwink, R. Černý, D. B. Ravnsbæk, Y. Filinchuk, M. Dornheim, F. Besenbacher and T. R. Jensen, *Chem. Soc. Rev.*, 2017, **46**, 1565–1634.
20 W. S. Tang, M. Matsuo, H. Wu, V. Stavila, W. Zhou, A. A.

Talin, A. V Soloninin, R. V Skoryunov, O. A. Babanova, A. V Skripov, A. Unemoto, S.-I. Orimo and T. J. Udovic, *Adv. Energy Mater.*, 2016, **6**, 1502237.

21 W. S. Tang, M. Dimitrievska, V. Stavila, W. Zhou, H. Wu, A. A. Talin and T. J. Udovic, *Chem. Mater.*, 2017, **29**, 10496–10509.

22 T. J. Udovic, M. Matsuo, A. Unemoto, N. Verdal, V. Stavila, A. V. Skripov, J. J. Rush, H. Takamura and S. I. Orimo, *Chem. Commun.*, 2014, **50**, 3750–3752.

23 Z. Jian, W. Luo and X. Ji, *J. Am. Chem. Soc.*, 2015, **137**, 11566–11569.

24 B. L. Ellis and L. F. Nazar, *Curr. Opin. Solid State Mater. Sci.*, 2012, **16**, 168–177.

25 S. Payandeh, R. Asakura, P. Avramidou, D. Rentsch, Ł. Zbigniew, C. Radovan, A. Remhof and C. Battaglia, *Chem. Mater.*, 2020, **32**, 1101–1110.

26 G. B. Dunks, K. Barker, E. Hedaya, C. Hefner, K. Palmer-Ordonez and P. Remec, *Inorg. Chem.*, 1981, **20**, 1692–1697.

27 E. L. Muetterties, J. H. Balthis, Y. T. Chia, W. H. Knoth and H. C. Miller, *Inorg. Chem.*, 1964, **3**, 444–451.

28 F. Klanberg and E. L. Muetterties, in *Inorganic Syntheses, Volume XI*, ed. W. L. Jolly, McGraw-Hill Book Company, New York, Volume XI., 1968, pp. 24–32.

29 V. D. Aftandilian, H. C. Miller, G. W. Parshall and E. L. Muetterties, *Inorg. Chem.*, 1962, **1**, 734–737.

30 N. S. Hosmane, J. R. Wermer, Z. Hong, T. D. Getman and S. G. Shore, *Inorg. Chem.*, 1987, **26**, 3638–3639.

31 H. C. Miller, N. E. Miller and E. L. Muetterties, *Inorg. Chem.*, 1964, **3**, 1456–1463.

32 L. V. Titov, L. V. Zhemchugova, L. A. Gavrilova and P. V. Petrovskii, *Russ. J. Inorg. Chem.*, 2005, **50**, 1215–1217.

33 O. Volkov, K. Radacki, P. Paetzold and X. Zheng, *Zeitschrift für Anorg. und Allg. Chemie*, 2001, **627**, 1185–1191.

34 Y. Marcus, *J. Chem. Phys.*, 2012, **137**, 154501.

35 J. Mähler and I. Persson, *Inorg. Chem.*, 2012, **51**, 425–438.

36 L. A. Leites, *Chem. Rev.*, 1992, **92**, 279–323.

37 D. Sethio, L. M. Lawson Daku and H. Hagemann, *Int. J. Hydrogen Energy*, 2017, **42**, 22496–22501.

38 E. A. V. Ebsworth and N. Sheppard, *Spectrochim. Acta*, 1959, **13**, 261–270.

39 P. Broadhead and G. A. Newman, *Spectrochim. Acta Part A Mol. Spectrosc.*, 1972, **28**, 1915–1923.

40 B. Hribar, N. T. Southall, V. Vlachy and K. A. Dill, *J. Am. Chem. Soc.*, 2002, **124**, 12302–12311.

41 D. Sveinbjörnsson, J. S. G. Myrdal, D. Blanchard, J. J. Bentzen, T. Hirata, M. B. Mogensen, P. Norby, S. I. Orimo and T. Vegge, *J. Phys. Chem. C*, 2013, **117**, 3249–3257.

42 S. Kim, N. Toyama, H. Oguchi, T. Sato, S. Takagi, T. Ikeshoji and S. I. Orimo, *Chem. Mater.*, 2018, **30**, 386–391.

43 R. Černý, M. Brighi and F. Murgia, *Chemistry*, 2020, **2**, 805–826.

44 N. Kamaya, K. Homma, Y. Yamakawa, M. Hirayama, R. Kanno, M. Yonemura, T. Kamiyama, Y. Kato, S. Hama, K. Kawamoto and A. Mitsui, *Nat. Mater.*, 2011, **10**, 682–686.

45 A. Gradišek, M. Krnel, M. Paskevicius, B. R. S. Hansen, T. R. Jensen and J. Dolinšek, *J. Phys. Chem. C*, 2018, **122**, 17073–17079.

46 J. B. Grinderslev, K. T. Møller, Y. Yan, X. M. Chen, Y. Li, H. W. Li, W. Zhou, J. Skibsted, X. Chen and T. R. Jensen, *Dalt. Trans.*, 2019, **48**, 8872–8881.

47 Y. Sadikin, R. V. Skoryunov, O. A. Babanova, A. V. Soloninin, Z. Lodziana, M. Brighi, A. V. Skripov and R. Černý, *J. Phys. Chem. C*, 2017, **121**, 5503–5514.

48 M. Dimitrievska, H. Wu, V. Stavila, O. A. Babanova, R. V. Skoryunov, A. V. Soloninin, W. Zhou, B. A. Trump, M. S. Andersson, A. V. Skripov and T. J. Udovic, *J. Phys. Chem. C*, 2020, **124**, 17992–18002.

49 W. S. Tang, M. Matsuo, H. Wu, V. Stavila, A. Unemoto, S. I. Orimo and T. J. Udovic, *Energy Storage Mater.*, 2016, **4**, 79–83.

50 M. N. Guzik, R. Mohtadi and S. Sartori, *J. Mater. Res.*, 2019, **34**, 877–904.

51 K. T. Møller, M. Paskevicius, J. G. Andreasen, J. Lee, N. Chen-Tan, J. Overgaard, S. Payandeh, D. S. Silvester, C. E. Buckley and T. R. Jensen, *Chem. Commun.*, 2019, **55**, 3410–3413.

52 S. Tang and H. Zhao, *RSC Adv.*, 2014, **4**, 11251–11287.

53 Y. Yan, J. B. Grinderslev, Y. S. Lee, M. Jørgensen, Y. W. Cho, R. Černý and T. R. Jensen, *Chem. Commun.*, 2020, **56**, 3971–3974.

54 T. J. Udovic, M. Matsuo, W. S. Tang, H. Wu, V. Stavila, A. V Soloninin, R. V Skoryunov, O. A. Babanova, A. V Skripov, J. J. Rush, A. Unemoto, H. Takamura and S. Orimo, *Adv. Mater.*, 2014, **26**, 7622–7626.

55 V. Lacivita, Y. Wang, S. H. Bo and G. Ceder, *J. Mater. Chem. A*, 2019, **7**, 8144–8155.

56 R. Asakura, L. Duchêne, R. S. Kühnel, A. Remhof, H. Hagemann and C. Battaglia, *ACS Appl. Energy Mater.*, 2019, **2**, 6924–6930.

57 R. Asakura, D. Reber, L. Duchêne, S. Payandeh, A. Remhof, H. Hagemann and C. Battaglia, *Energy Environ. Sci.*, 2020, **13**, 5048–5058.

58 L. Zhang, D. Zhang, K. Yang, X. Yan, L. Wang, J. Mi, B. Xu and Y. Li, *Adv. Sci.*, 2016, **3**, 1–6.

59 W. S. Tang, K. Yoshida, A. V. Soloninin, R. V. Skoryunov, O. A. Babanova, A. V. Skripov, M. Dimitrievska, V. Stavila, S. I. Orimo and T. J. Udovic, *ACS Energy Lett.*, 2016, **1**, 659–664.

60 L. Duchêne, R. S. Kühnel, D. Rentsch, A. Remhof, H. Hagemann and C. Battaglia, *Chem. Commun.*, 2017, **53**, 4195–4198.

61 Y. Sadikin, M. Brighi, P. Schouwink and R. Černý, *Adv. Energy Mater.*, 2015, **5**, 1501016.

62 W. S. Tang, A. Unemoto, W. Zhou, V. Stavila, M. Matsuo, H. Wu, S. ichi Orimo and T. J. Udovic, *Energy Environ. Sci.*, 2015, **8**, 3637–3645.

63 A. Unemoto, K. Yoshida, T. Ikeshoji and S. I. Orimo, *Mater. Trans.*, 2016, **57**, 1639–1644.

64 L. He, H. Li, H. Nakajima, N. Tumanov, Y. Filinchuk, S. Hwang, M. Sharma, H. Hagemann and E. Akiba, *Chem. Mater.*, 2015, **27**, 5483–5486.